Available online at www.sciencedirect.com

SciVerse ScienceDirect

Acta Materialia 61 (2013) 1872–1885

Acta MATERIALIA

www.elsevier.com/locate/actamat

Emergence of enhanced strengths and Bauschinger effect in conformally passivated copper nanopillars as revealed by dislocation dynamics

Seok-Woo Lee *, Andrew T. Jennings, Julia R. Greer

Division of Engineering and Applied Science, California Institute of Technology, 1200E. California Blvd., Pasadena, CA 91125, USA

Received 27 October 2012; received in revised form 6 December 2012; accepted 6 December 2012
Available online 16 January 2013

Abstract

The ability to precisely control the surface state of a nanostructure may offer a pathway towards tuning the mechanical properties of small-scale metallic components. In our previous work [Jennings et al., Acta Mater. 60 (2012) 3444–3455], single-crystalline Cu nanopillars were conformally coated with a 5–25 nm thick layer of TiO_2/Al_2O_3. Uniaxial compression tests revealed two key findings associated with these passivated samples: (i) ~80% higher strengths as compared with the uncoated samples of the same diameter, 200 nm; and (ii) Bauschinger effect-like hysteresis during unloading–reloading segments. Dislocation dynamics simulations of uniaxially compressed 200 nm diameter Cu nanopillars with coated surfaces revealed the contribution of dislocation multiplication, pinning, and pile-up processes to the experimentally observed enhancement in pillar strength. They further helped explain the transition of plasticity mechanisms from dislocation multiplication via the operation of single-arm dislocation sources to dislocation nucleation from the crystal-coating interface. Hysteresis in stress–strain data is discussed in the framework of dislocation structure evolution during unloading–reloading cycles in experiments and simulations.

Keywords: Plasticity; Dislocation; Dislocation dynamics; Dislocation density; Coating

1. Introduction

Understanding dislocation behavior at small length scales is important not only for acquiring new fundamental knowledge of small-scale plasticity, but also for the design of reliable nano- or microelectromechanical systems (NEMS/MEMS) and small-scale components [1]. When the external material dimensions are comparable to the internal material microstructural length scales, the mechanical properties have been shown to deviate from those of microstructurally similar materials with macroscopic dimensions [2–7]. Thus, the macroscale mechanical properties, frequently tabulated and widely reported in the literature, cannot accurately describe material properties at the micron- and submicron scales. In the last decade, small-scale plasticity has been extensively explored using micro- or nanopillar compression/tension tests predominantly in single-crystalline metals [8–10]. These reviews, as well as references therein, ubiquitously observe the "smaller is stronger" trend in nano- and microsized single-crystalline metals, whereby smaller samples require the application of higher stresses to deform plastically. While the specific mechanisms explaining such size-dependent mechanical behavior are a matter of ongoing discussion, it is generally agreed that the plasticity in single-crystalline metals at small length scales is controlled by the intermittent operation of dislocation sources, also known as nucleation- or source-controlled plasticity [8–10].

Size-dependent strength and a stochastic signature in the stress–strain data during plastic flow represent two

* Corresponding author. Tel.: +1 650 799 1566; fax: +1 626 395 8868.
E-mail address: swlee49@caltech.edu (S.-W. Lee).

1359-6454/$36.00
http://dx.doi.org/10.1016/j.actamat.2012.12.008

key characteristics of the source-controlled plasticity. The size-dependent strength, or a "smaller is stronger" phenomenon, has been reported for a wide variety of face-centered and body-centered, as well as hexagonal closed-packed metallic samples, shaped into cylindrical geometries and uniaxially strained [10]. Generally, their strengths have the functional form of a power law, $\sigma = A \cdot D^{-n}$, where σ is the flow or yield stress in tension or compression, A is a proportionality constant, D is the pillar diameter, and n is the power-law exponent that depends on material, microstructure and crystallographic orientation [8]. The emergence of such enhanced strengths at small length scales may be beneficial in the design of small-scale structures, which would be capable of supporting high stresses before permanently deforming or failing. However, the concurrent jerky plastic stress–strain behavior, often exhibited by shearing small-scale metals, may be problematic in design because the discrete strain bursts occur stochastically at ill-defined stresses, and cause difficulties in controlling homogeneous plastic forming [11–16]. This uncertainty in the commencement of material deformation may lead to a sudden and catastrophic collapse of the components comprising a device, which would lead to its failure. Strain bursts are thought to be a result of one or more mobile dislocations being released from their pinned positions and annihilating at the free surfaces in an avalanche-like fashion. In the course of plastic deformation, some of the remaining mobile dislocations become pinned and then operate intermittently as single-arm dislocation sources, which subsequently produce strain bursts. This type of plasticity, where strain is carried by the operation of single-arm sources (SASs), has been widely observed in micron-sized metals [17–22]. It has been reported that in smaller crystals, with dimensions well below 1 μm, the avalanches may be driven by dislocations nucleating at the free surfaces of the nanocrystals and subsequently annihilating or becoming pinned [23–25]. Irrespective of these differences in the initial dislocation positions—either emanating from an internal network of pinning points or originating at the surface—the substantial ratio of the free surface area to volume in small-sized crystals enables the dislocation to annihilate at the surface upon mechanical loading. Therefore, it is reasonable to expect that a modification of the sample surface would affect these mechanisms, which strongly depend on the dislocation annihilation and nucleation rates, as well as on their nucleation stresses. For instance, the influence of hard conformal coatings on the deformation of single-crystalline nanopillars and thin films has been explored as a means to alter the surface state and mechanical responses [26,27].

It has been experimentally demonstrated that coating small-scale single-crystalline metallic cylinders suppressed the discrete nature of their compressive stress–strain data and resulted in enhanced strengths and in significant storage of dislocations. For example, it was found that Al_2O_3-coated Au nanopillars with diameters of 500–900 nm showed 100% higher flow stresses at 10% strain, as well as a transition from discrete plastic flow in the uncoated pillars to a continuous plastic flow and hardening in the coated ones [28]. Ng and Ngan reported similar observations in W–Ga alloy-coated Al micropillars with diameters of ~6 μm. They performed transmission electron microscopy of deformed coated Al micropillars and found that the dislocation density increases up to $10^{15}\ m^{-2}$ [29]. Recently, the current authors conformally coated 5–25 nm thick TiO_2/Al_2O_3 onto single-crystalline Cu nanopillars with diameters between 75 nm and 1 μm by using atomic layer deposition (ALD) [27]. Uniaxial compression tests revealed that 200 nm diameter coated samples reached ~80% higher maximum strengths (1129 ± 201 MPa) than the uncoated ones with equivalent diameters (619 ± 66 MPa). Coated samples of all diameters collapsed via a single, substantial strain burst, on the order of 0.1–0.3, followed by the cracking of the coating. In addition, ALD coated samples had a hysteresis loop in the unloading–reloading cycles during plastic flow, a phenomenon also known as the Bauschinger effect.

In that experimental work, the underlying physical mechanisms giving rise to the enhanced strengths and the Bauschinger effect in the coated nanopillars were explained through classical dislocation theory, which is not capable of capturing some of the key details associated with the interactions and motion of individual dislocations. In the work presented here, we performed three-dimensional (3-D) dislocation dynamics (DD) simulations to obtain a more detailed physical insight into the effects of hard conformal coatings on metallic nanostructures on dislocation behavior. Several existing DD-based studies have explored the effects of coatings on the mechanical properties of cylindrical micropillars and 2-D thin films [26,30,31]. In those reports, the samples had relatively low initial dislocation densities, $\sim 10^{12}\ m^{-2}$, and the dislocation structures contained a number of pre-positioned, non-destructible dislocation pinning points. Such a condition of "immortality" of a dislocation source could result in overestimating the number of generated dislocations, resulting in an artificial increase in dislocation density. In this work, we focused on studying the dislocation activity in 200 nm diameter uncoated and coated Cu nanopillars, without the pre-planted pinning points, and utilizing the experimentally measured initial dislocation density of $\sim 10^{14}\ m^{-2}$ [27]. The contribution of dislocation pile-ups to the overall strength in coated pillars was determined by calculating the dislocation density at the maximum experimentally measured stress. We also performed the unloading–reloading simulations to examine Bauschinger-like hysteresis curves in detail. These simulations along with the scanning and transmission electron microscopy (SEM and TEM) analysis of the post-deformed sample morphologies bring to light the potential mechanisms responsible for the large post-maximum stress–strain bursts and the Bauschinger effect emergent in the passivated nanostructures.

2. Simulation set-up

2.1. Image stress calculation and boundary conditions

We used the Parallel Dislocation Simulator (ParaDiS), originally developed at Lawrence Livermore National Laboratory [32]. This code was modified to adapt a cylindrical geometry [33], and the Yoffe image stress was used to calculate the image stress imposed by the free surfaces in the as-fabricated pillars and by the pillar/coating interface in the coated pillars. The Yoffe image stress is the image stress for a semi-infinite straight dislocation terminated at the free surface of the elastic half-space [34]. In sufficiently small sample volumes it is reasonable to expect that most dislocations were terminated at the free surface rather than at an internal sink. Therefore, the Yoffe image stress could roughly estimate the image stresses of the truncated dislocation networks and has been shown to work particularly well for a surface segment [35]. To calculate the image stress field more precisely, the spectral method or the finite-element method would need to be incorporated together [35,36], which is cumbersome and non-trivial, especially for the cases involving hard coatings. The focus of this work was to describe the fundamentals of the dislocation source operation and ensuing dislocation processes, which occurred at relatively high stresses, rendering the Yoffe image stress analysis suitable. The Yoffe image stress analysis is also advantageous because it has an analytical solution, which leads to it having a higher computation efficiency compared with other methods.

Similar to previous studies, the surface layer in the coated pillars was modeled as an impenetrable boundary [30,31]. Since the ALD Al_2O_3/TiO_2 coating is a strong ceramic material, treating it as a boundary impenetrable by dislocations was a reasonable choice. Our experiments revealed that the nanocracks were sometimes generated along the axial direction of the pillar, presumably driven by the hoop stresses induced by the presence of a coating. These cracks were generally formed after attaining the maximum strength, which suggests that these simulations may adequately reflect the dislocation processes prior to sample failure [27]. Thus, this impenetrable boundary condition was applied until failure, defined as the stress at which the final catastrophic strain burst occurred in experiments. To incorporate the impenetrable boundary condition into the computational code, the mobility law of a node, especially the ones closest to the free surface, was given special treatment. Any node located within $5\times$ the magnitude of the Burgers vector ($5b = 1.3$ nm) from the free surface was considered to be in the surface proximity. This threshold range of $5b$ was sufficiently small to produce dislocation pile-ups just near the free surface. For a node within this range, if the direction of the nodal force vector contained an outward radial component, its mobility vanished; otherwise, the mobility remained unchanged. Using this algorithm enabled not only the dislocation pile-ups but also the Bauschinger effect to be captured; the dislocations near the pillar exterior were unable to escape at the surface, but could move inward and drive a reversed plastic flow. During intentional unloading from a particular flow stress, both the back-stresses and the line tension force allowed the dislocations to move in the direction opposite to that dictated by the Peach–Koehler force of applied stress, resulting in a different stress–strain path during unloading vs. reloading, i.e. the Bauschinger effects (Fig. 4 in this paper or Fig. 2 in Ref. [27]). This boundary condition does not include the effect of the repulsive image stress caused by the strain compatibility requirement at the interface between the pillar and the coating, which could lead to an underestimation of the total image force. In the course of this work we discovered that this combination of the back-stresses and the line tension force was sufficient to observe a notable Bauschinger effect, comparable with experimental observations. Thus, this impenetrable boundary condition appears to serve as a reasonable framework for studying the Bauschinger effect. More discussion about the image stress and the impenetrable boundary condition is available in the Supplementary material.

2.2. Loading scheme and mobility parameters

Loading was imposed via a cut-off plastic strain rate method, where a constant increment of 0.05 MPa was applied at every simulation step, as was commonly done in other DD simulations [19,30,31,37]. The code calculates the total plastic strain rate for each time step, and if this plastic strain rate became higher than the pre-assigned cut-off value, the load was kept constant until the plastic strain rate shifted to below this threshold. This method allows us to mimic the experimental stress–strain response measured by a load-controlled machine, which is commonly used. In other DD studies, the cut-off plastic strain rate was usually chosen as the elastic strain rate, which depends on the magnitude of mobility parameters. For face-centered cubic (fcc) crystals, the elastic strain rate usually ranges from 10^2 to 10^6 s^{-1} in DD simulations. For this particular geometry of $D \sim 200$ nm nanopillars and the common fcc mobility parameter of $M_{edge} = M_{screw} = 10^4$ Pa s [38,39], we found that the plastic cut-off strain rate, 5×10^4 s^{-1}, is the optimum value to distinguish between the real plastic strain burst and the noise amplitude. In the course of this work we discovered that this method produced stress–strain curves that were insensitive to the loading rate because varying the loading increments by one order of magnitude, i.e. 0.005 MPa per each time step, produced results almost identical to those obtained using 0.05 MPa per time step. Since the operation stress of single-arm dislocation source is determined by the sample geometry (here, the diameter, D) rather than the dislocation mobility, the stress–strain response of the cut-off plastic strain rate method is relatively loading rate insensitive (or equivalently strain-rate insensitive). A similar strain-rate insensitivity was observed in other DD studies with a similar mobility parameter [39,40]. Experiments also

showed that the operation stress of single-arm dislocation source is relatively insensitive to the strain rate of 10^{-1}–10^{-3} s^{-1} [41]. Such a lack of rate sensitivity in our cut-off plastic strain-rate method indicates that the calculated stress–strain curves could be compared to the experimental data, which was typically measured at a lower loading or displacement rate [39].

We studied eight cylindrical samples with a diameter of 200 nm and a height of 600 nm with materials parameters of Cu (shear modulus 44 GPa, Poisson's ratio 0.415.). The z-axis (loading axis) of the sample was positioned along its [0 0 1] direction, as opposed to [1 1 1] as in the experiments, and the simulation cell was periodic along the z-direction. The effect of the orientation will be taken into account in data analysis when comparing simulations with experimental results. The fcc linear mobility law included both a glide and a line constraint. The glide constraint allows a dislocation to move only on its slip plane to mimic the effect of the extended core structures of dislocations in fcc crystals, and the line constraint makes a Lomer–Cottrell (LC) junction immobile in the direction perpendicular to the line in order to take its non-planar core structure into account [42].

2.3. Cross-slip scheme

Cross-slip was modeled such that a screw dislocation segment located at the intersection of two slip planes moved along the higher projected force direction among these two slip planes. First, a nodal force was evaluated for each possible slip plane. If a projected nodal force on any of the other slip planes exceeded that on the current slip plane, and if the dislocation segment had screw character, the node was temporarily placed into the new slip plane. The nodal force was then evaluated again to assess whether it would drive the dislocation further on the new slip plane: if this is the case, the code allows a cross-slipped segment to stay on a new slip plane. Otherwise, the code brings the segment back to the original position and forces the segment to move on the original slip plane. Such a formulation causes the cross-slip to occur more frequently than would be expected because it does not account for the probabilistic nature of cross-slip attempts. Such an over-production of cross-slip has been useful in revealing the limit of dislocation multiplication induced by cross-slip in a small volume.

Cross-slip was temporarily disabled during the formation of the initial dislocation substructure, which was done by relaxing the randomly distributed dislocation loops. Such an algorithm for creating the initial microstructure was particularly useful for ascertaining whether a stable dislocation network could be formed even in the absence of cross-slip, unlike in many other DD studies [43]. The cross-slip process was subsequently enabled during straining simulations because it represents a physical mechanism for the multiplication of dislocations in coated nanopillars under an externally applied stress [30,31].

3. Results

3.1. Sample geometry and initial dislocation structure

The initial dislocation landscape was produced by the relaxation of randomly created dislocation loops, following an approach similar to that in Ref. [43]. In this methodology, the dislocation structures were relaxed in the absence of applied stress until the dislocation density remained unchanged. Fig. 1a shows the sample geometry and the dislocation arrangements before and after relaxation. The dislocation density profile in Fig. 1 shows that the dislocation structures were fully relaxed after a sufficiently large number of time steps, ~350,000 steps. One distinction of this method from that of Ref. [43] is that no cross-slip processes were allowed to occur during relaxation in order to assess the possibility of forming pinning points in the absence of cross-slip, as suggested by the geometrical study in Ref. [20]. Indeed, strong pinning points were naturally formed via the mutual interactions of three dislocations. A snapshot and a schematic of such a triple dislocation interaction, leading to the formation of a LC junction, are shown in Fig. 1b and c. Such a natural formation of rigidly pinned junctions is in contrast to the commonly used random initial distributions of the pinning points used in many DD simulations [30,31]. Fig. 1c shows three dislocations to be rigidly pinned around point B as a result of the glide (dislocations (2) and (3)) and line (LC dislocation) constraints of fcc mobility law described in Section 2.2. Such interactions form stable dislocation networks in a natural way, and hence do not have to rely on the random distributions of pre-pinned locations, which are often not representative of realistic material microstructure. These types of triple-dislocation interactions rarely occur at low dislocation densities (both line length and number) because it requires a special sequence of dislocation interactions to occur—such as the formation of an LC junction followed by dislocation annihilation (or vice versa). A stable dislocation network was formed even without cross-slip because we chose a relatively high dislocation density of 5–6×10^{14} m^{-2} before relaxation. Eight relaxed dislocation structures, each with the dislocation density close to the experimentally measured values, 1–2×10^{14} m^{-2}, were created for the straining study [27].

3.2. Stress–strain curves of uniaxial compression simulations

3.2.1. Uncoated Cu nanopillars with diameters $D \sim 200$ nm

Fig. 2a portrays eight stress–strain curves of $D \sim 200$ nm uncoated Cu nanopillars with initial dislocation densities of 1–2×10^{14} m^{-2}. The step-like signature in the stress–strain curves is attributed to the dislocation source exhaustion hardening, as commonly observed in the literature [19]. The premise of source exhaustion hardening is that during plastic loading, the single-arm dislocation sources cease operating when they either interact with other dislocations or annihilate at the free surface [37]. To

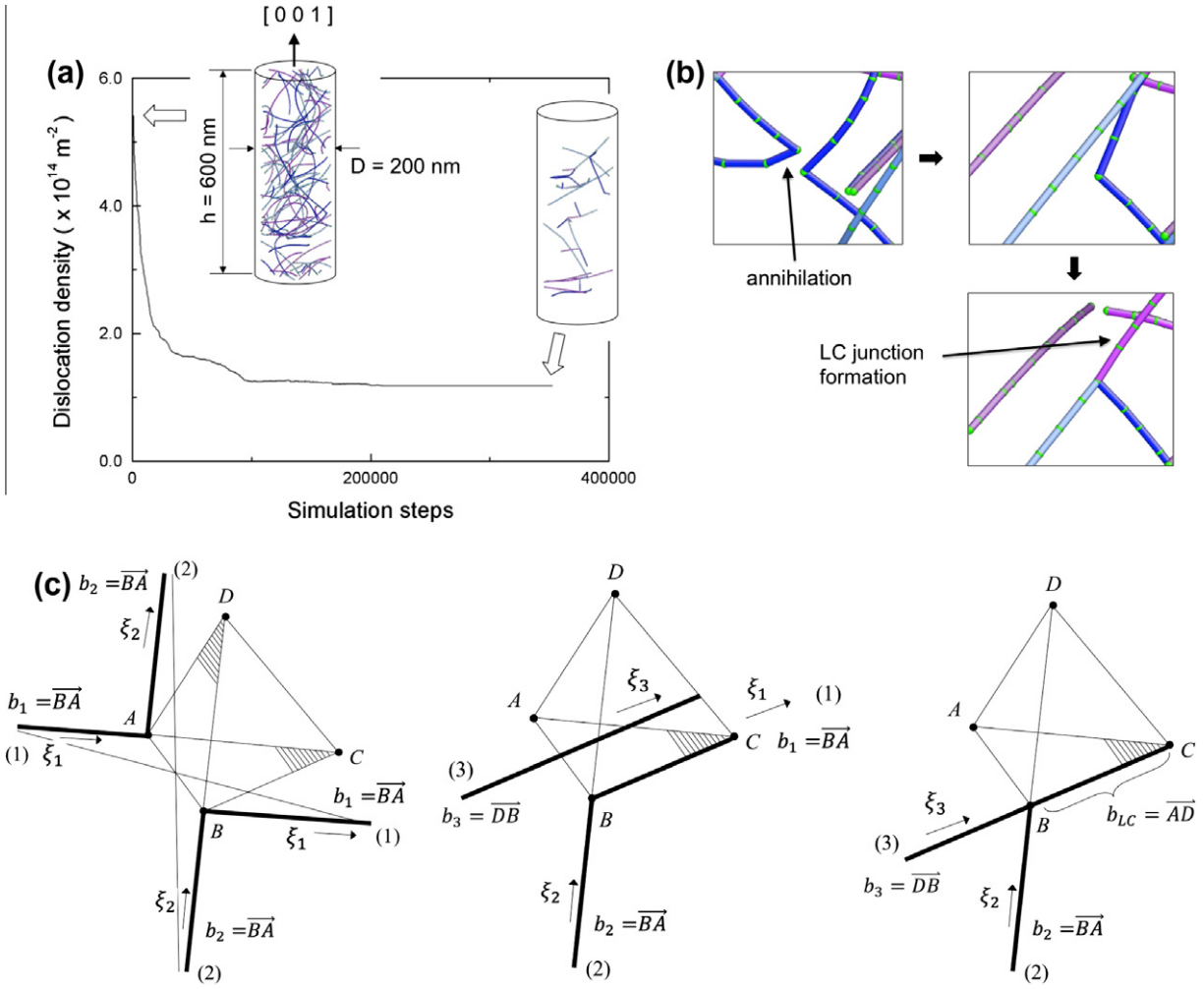

Fig. 1. (a) Simulation snapshots of dislocation structures before and after relaxation, and the dislocation density profile during relaxation. (b) Triple dislocation interaction that produces a dislocation pinning point. (c) Schematic diagram of the triple dislocation interaction shown in (b). The first one shows dislocation annihilation between the point A and B, and the third one shows the formation of a Lomer–Cottrell junction.

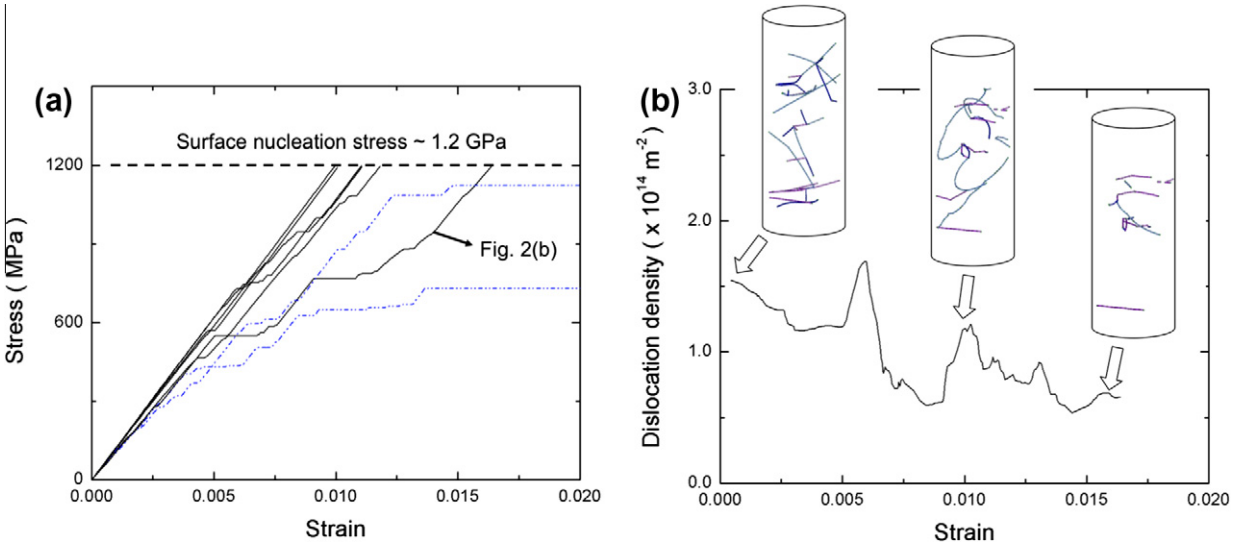

Fig. 2. (a) Stress–strain curves of $D \sim 200$ nm uncoated Cu nanopillars. (b) Simulation snapshots of dislocation structures and the dislocation density profile of the sample designated in (a) during uniaxial compression. Surface nucleation stress (1.2 GPa) in (a) is estimated from the literature [27].

continue plastic deformation, higher stresses need to be applied to activate stronger dislocation sources, which continue to carry plasticity at higher stresses. Fig. 2b illustrates the dislocation density profile and the corresponding snapshots of the sample shown in Fig. 2a, both of which are typical for the free surface-bounded nanocylinders. In the simulations presented here, most of the dislocation sources formed and disappeared dynamically. In the plot, the six pillars denoted by the black solid lines hardened more rapidly than the remaining two pillars, shown as blue dotted lines. In the cases where the so-called dynamic dislocation sources became exhausted in the early stages of the loading, the existing dislocations could not accommodate the prescribed loading rate, which resulted in the immediate and substantial flow stress increase. Here, a dynamic dislocation source means that its pinning point is not static, i.e. is not fixed in location or in time as discussed in Ref. [43]. The resulting strain-hardening rate in the stress–strain curve depends on both the initial dislocation structures and on the rate of source exhaustion. These results and arguments agree well with existing DD studies [19,43].

The stresses to nucleate dislocations from the described single-arm sources are not arbitrarily high and have an upper bound, which is determined by the stress that enables dislocation nucleation from the free surfaces. For Cu, existing experimental results demonstrated that dislocation nucleation from free surfaces occurs at stresses of the order of 1 GPa. Jennings et al. measured the surface nucleation stress for a series of different strain rates and showed that for the compressive strain rates of 10^{-2}–10^{-3} s^{-1}, the surface nucleation stress of ⟨1 1 1⟩-oriented Cu nanopillars was ~1 GPa [41]. Computations by Zhu et al. estimated the surface nucleation stress of [0 0 1]-oriented Cu nanopillars to be ~1.3 GPa at 300 K for the strain rate of 10^{-3} s^{-1}, using the free end nudged elastic band method and transition state theory for a Cu nanowire [44]. The differences in the specific experimental conditions and computational setup have resulted in a range of the reported surface nucleation stresses. However, they are generally of the order of 1 GPa of Cu, and for the simulations in this work we took the surface nucleation stress to be 1.2 GPa. Thus, the DD simulations in Fig. 2 were terminated when the applied stress reached this threshold since it is, in reality, difficult to obtain stress levels higher than the dislocation nucleation stress.

Based on this limiting strength criterion, it is reasonable to expect that beyond the strain of 0.01% (Fig. 2a), the deformation may be facilitated by either the operation of either the SASs or the surface sources (SSs) for $D \sim 200$ nm Cu nanopillars. This observation agrees with the reported mechanistic transition from SAS to SS operation in uncoated Cu nanopillars, whose initial dislocation density was similar to that investigated in this study [41]. Jennings et al. showed that the transition diameter between these two different plasticity mechanisms occurred at ~200 nm. Thus, our choice of simulation conditions and the surface nucleation threshold appears to be reasonable in terms of capturing the physical phenomena observed experimentally.

3.2.2. Coated Cu nanopillars with diameters $D \sim 200$ nm

Fig. 3a shows the compressive stress–strain curves for the Cu nanopillars with impenetrable coatings described in Section 2.1. It is evident that the presence of a coating does not fully suppress the stochastic signature in the stress–strain behavior: multiple small strain bursts are present throughout the deformation. The extent and duration of these bursts, however, appears to be significantly reduced as compared with the stress–strain curves for the uncoated pillars shown in Fig. 1a. In addition, the strain-hardening rate in the passivated samples is higher than it is in the uncoated nanopillars. It is likely that the increased hardening rate may be due to the dislocations piling-up near the pillar surface–coating interface, which leads to the more rapid "shutting down" of the operating SASs and to the quick subsequent activation of additional, harder sources.

The dislocation density profile shown in Fig. 3b indicates that the dislocation density increased to 3.7×10^{14} m^{-2}, which is about three times higher than the initial dislocation density. For comparison, the dislocation density profile of a representative uncoated nanopillar with the same initial dislocation structure is also depicted on the same plot. The dislocation structures (Fig. 3b) and the cross-slip schematic (Fig. 3c) reveal that the dominant dislocation multiplication mechanisms in the passivated nanopillars were (i) dislocation pile-up and (ii) cross-slip. Although the DD simulations revealed the final overall increase in the dislocation density to be marginal, a factor of ~3–4, TEM analysis from the authors' previous experimental study (Fig. 5b) showed a more significant increase in the dislocation density in the coated samples, of the order of 10–20 [27]. A streaky diffraction pattern (Fig. 6b) was also observed, which suggests that low-angle grain boundaries were formed that result from the significant increase in dislocation density. This discrepancy could have come from another plasticity mechanism that DD simulations cannot yet capture.

3.3. Bauschinger effect

Fig. 4a shows a plot of the stress vs. strain data for a typical simulation, with an intentional unloading–reloading schedule. The sample was unloaded at 0.4% and 0.95% strains, and then reloaded once the load was reduced to 10% of its peak value within each cycle. The stress–strain curve reveals the presence of a hysteresis loop (Fig. 4a), as well as the dislocation density fluctuations (Fig. 4b), during these reverse-loading segments. No significant increase in dislocation density was observed even after the second unloading. The hysteresis was negligible during the first unloading–loading cycle, as shown in the zoomed-in data selection in the inset of Fig. 4a. In the second unloading–loading cycle, however, the amount of hysteresis, similar

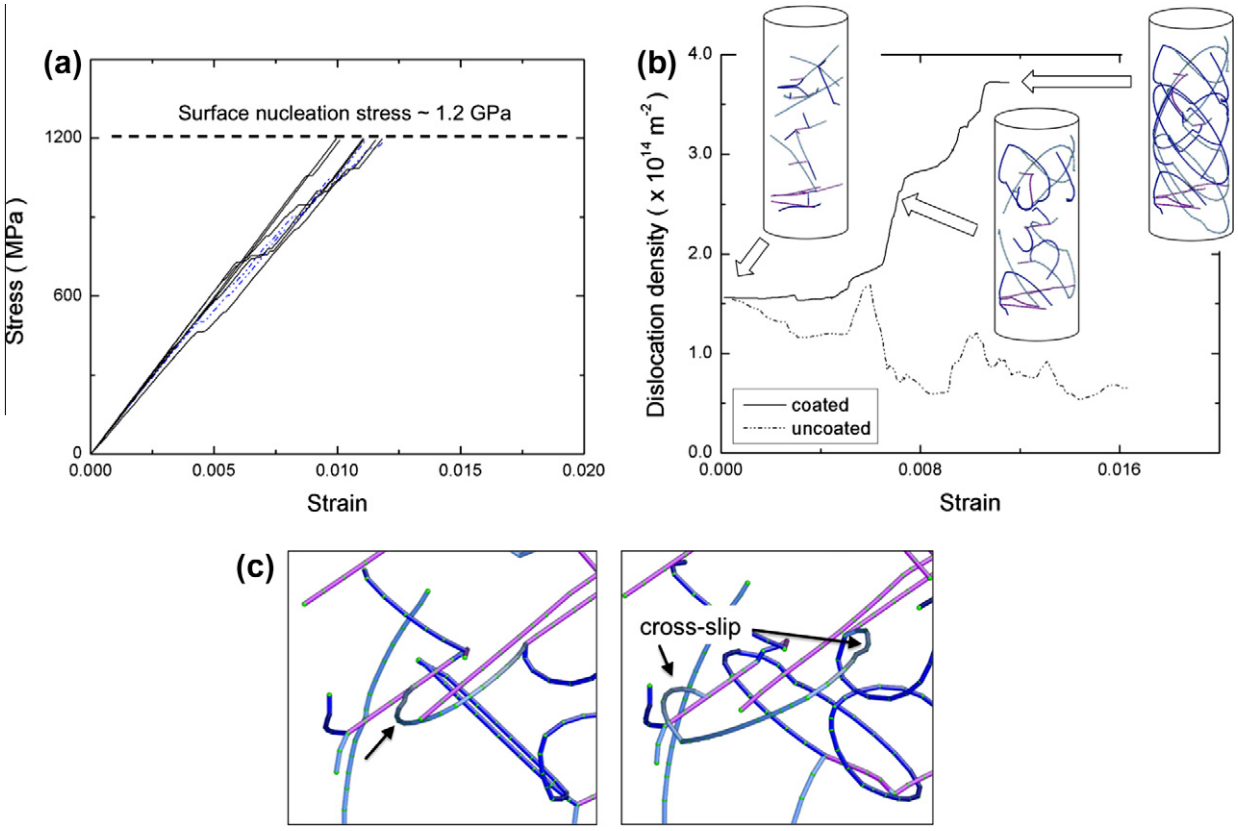

Fig. 3. (a) Stress–strain curves of $D \sim 200$ nm coated Cu nanopillars. (b) Simulation snapshots of dislocation structures and the dislocation density profile during uniaxial compression. The initial dislocation structure in these coated nanopillars is identical to that of the uncoated nanopillars of Fig. 2b. (c) Simulation snapshots before (left) and after (right) cross-slip. The dislocation segment indicated by the arrow in the left panel has cross-slipped after a few simulation steps, as illustrated in the right panel.

to the Bauschinger effect [27], is substantial. The first unloading occurred at relatively low strains, where the stress was not sufficiently high to produce dislocation pile-ups. Upon unloading, the backward plastic flow was insubstantial, which led to a weak distinction between the forward vs. reverse loading. When unloading from a higher strain, i.e. in the second cycle, the stress at the onset of unloading was a factor of ~2 higher than that in the first cycle, which is likely an indication of higher dislocation density. The Bauschinger effect was more pronounced in this case because of the substantial dislocation back-stresses. Fig. 4b shows the evolution of dislocation substructures, which include pile-ups and unraveling in the second cycle, as well as the calculated dislocation density, as a function of unloading–reloading cycle. A key distinction between the experimental data (Fig. 4c) and the simulations is that the first unloading–reloading curve in the experiments shows a noticeable Bauschinger effect. It is possible that dislocation pile-ups were generated even during the first cycle in the experiments, unlike in the DD simulations. The experimental stress–strain data also shows a lower hardening rate, as compared with simulations. The maximum stress in the simulations is attained at ~1.2% strain (Fig. 4a) while that in the experiment appears at ~5% (Fig. 4c). This implies that plastic deformation occurred at the initial stage of deformation in the experiments. This point is elaborated on in the Section 4.3.

4. Discussion

4.1. The contribution of dislocation pinning and pile-ups at the interface to the enhanced maximum strength

4.1.1. The behavior of single-arm dislocation sources in the presence of hard ceramic coating

In our previous work, we used a simple numerical method to estimate the dislocation densities in compressed $D \sim 200$ nm [1 1 1]-oriented single-crystalline Cu nanopillars coated with a thin conformal layer of TiO_2/Al_2O_3 [27]. We found that a dislocation density of 2.5×10^{15} m^{-2} was necessary to attain the experimentally obtained maximum strength of 1129 MPa. The underlying assumption of such a calculation was that the dislocation density increase was the only contributing factor to the higher strengths of the coated nanopillars. Ng and Ngan demonstrated the validity of this assumption for micron-sized Al samples by discovering that Taylor hardening alone could explain the enhanced strength of their coated pillars with the relatively large diameters of ~6 μm [29,45]. We also conjectured in our previous work that

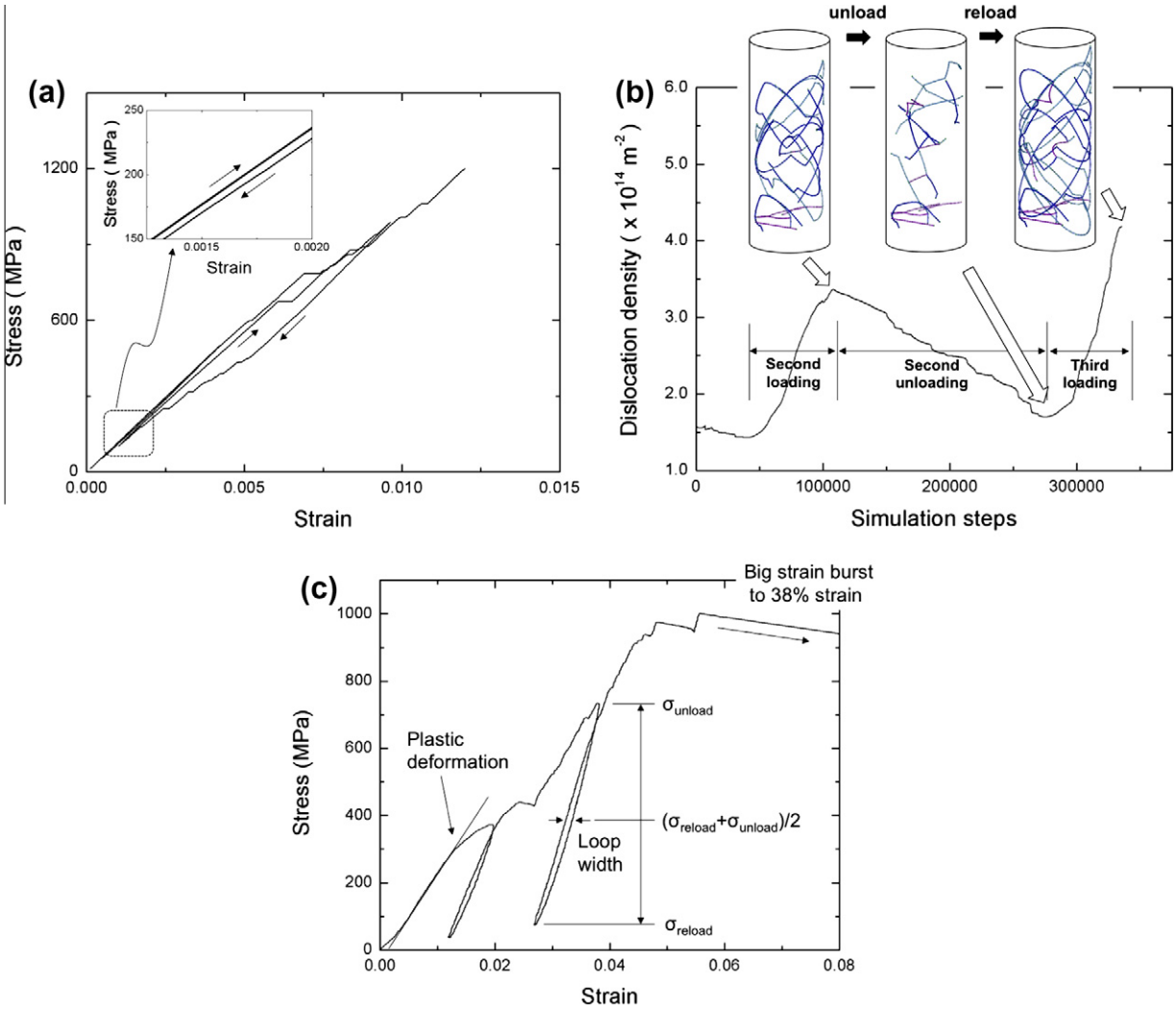

Fig. 4. (a) Stress–strain curve of $D \sim 200$ nm coated Cu nanopillar showing Bauschinger effects. The small arrows indicate unloading–reloading processes. (b) Simulation snapshots of dislocation structures and the dislocation density profile during cyclic loading processes. Note that the initial dislocation structure of this coated nanopillar is the same as that of the uncoated nanopillars in Fig. 2b and that of the coated nanopillars in Fig. 3b. Snapshots show the change of dislocation structures during the second cycle. (c) Experimental stress–strain curve of $D \sim 200$ nm coated Cu nanopillar. The loop width is used to compare the degree of Bauschinger effect between simulations and experiments.

the mechanism of dislocation cross-slip followed by pile-up against the interface could, in principle, give rise to such a high dislocation density [27]. However, the DD simulations in this work convey that a significant increase in dislocation density is not necessary to achieve the maximum stress (here, 1.2 GPa). As seen in Figs. 3b and 4b, the dislocation density increased only up to $\sim 4 \times 10^{14}$ m^{-2} from the initial value of $\sim 10^{14}$ m^{-2} upon compression to 1% strain. In the coated nanopillars, those dislocations that terminate at the interface become pinned by the hard ceramic coating, which requires the application of a higher stress because of the increased dislocation line tension contribution to the overall force. In addition, once the dislocations are piled-up against the interface, the back-stresses would impede the operation of dislocation sources.

Fig. 5a and b shows simple DD simulations for a single-arm source-driven plasticity in uncoated (Fig. 5a) vs. coated (Fig. 5b) samples. This single-arm dislocation source was created by positioning a stable pinning point at the center of pillar and then applying a constant tensile stress of 600 MPa. We discovered that the source operation stress of ~150 MPa for the uncoated nanopillar was nearly a factor of 4 lower than that for the coated nanopillar (~550 MPa). Hence, the dislocation pinning at the interface may significantly affect the source operation stress. We also found that the SAS in the uncoated sample rotated continuously (Fig. 5a), while it rotated only once in the coated samples before immobilizing, which was caused by the back-stresses generated by the initially piled-up segments (Fig. 5b). The last snapshot in Fig. 5b is the equilibrium configuration of the SAS under a tensile stress of 600 MPa. These results suggest that both the dislocation pinning at the interface and the dislocation pile-ups against the hard coating significantly contribute to the observed enhanced hardening in the coated nanopillars.

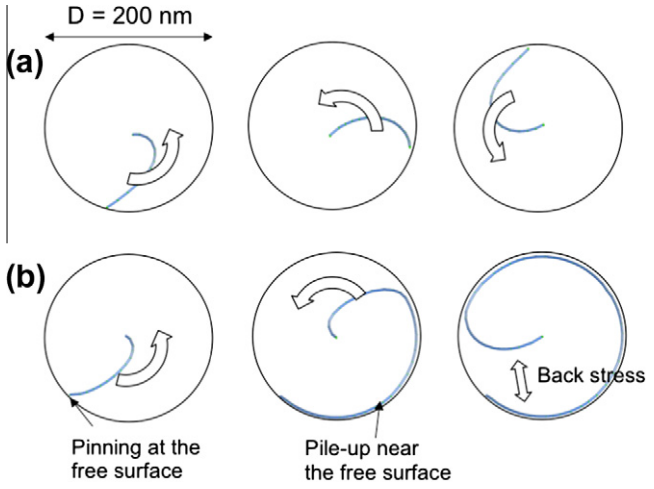

Fig. 5. The operation of dislocation source in (a) uncoated and (b) coated nanopillars under a tensile stress of 600 MPa. A single-arm source is artificially pinned at the center of pillar. The last snapshot in (b) is the equilibrium configuration. Thus, the back-stress prevents the operation of dislocation sources.

4.1.2. Numerical calculation of the coating contribution to the overall strength

To analyze the contribution of dislocation multiplication and pinning/pile-up to hardening, we used a modified form of the originally used SAS model [27]. A direct comparison of the stress–strain curves between uncoated and coated nanopillars cannot provide this type of information. Furthermore, the number of simulations may not be sufficient to obtain reasonable statistics. Thus, we used a DD-assisted SAS model and introduced a new term, which accounted for each of these processes: dislocation pinning and pile-up:

$$\sigma = \frac{1}{M}\left(\tau_0 + 0.5\mu b\sqrt{\rho_{tot}} + \frac{\mu b}{4\pi\lambda_i} ln\left(\frac{\lambda_i}{b}\right)\right) + \Delta\sigma_{coating} = \sigma_{SAS} + \Delta\sigma_{coating}, \quad (1)$$

where σ is the axial stress at the first strain burst, M the Schmidt factor, τ_0 the friction stress, μ the shear modulus, b the magnitude of the Burgers vector, ρ_{tot} the total dislocation density, λ_i the length of the ith single-arm dislocation source, σ_{SAS} the axial strength of the pillar without the coating, and $\Delta\sigma_{coating}$ the axial strength contribution of dislocation pinning and pile-up due to the existence of coating. The term $\Delta\sigma_{coating}$ can be regarded as the additional strengthening induced by the coating, as compared to the uncoated pillars. A detailed description of the numerical method is available in the supplementary information of Ref. [27].

Once we know the dislocation density at the maximum stress level, σ_{SAS} can be obtained following the method described in Ref. [27]. Then, $\Delta\sigma_{coating}$ can be estimated simply by $\Delta\sigma_{coating} = \sigma_{max,exp} - \sigma_{SAS}$, where $\sigma_{max,exp}$ is the experimentally measured maximum strength (1129 MPa). Thus, the dislocation density at the maximum stress level must be known in order to solve Eq. (1), and in fact, DD simulations provide this quantity. For the [0 0 1] loading direction, the DD simulations predicted a dislocation density of $4 \times 10^{14}\ m^{-2}$ at the maximum stress. To simulate realistic experimental conditions, we estimated the dislocation density for the [1 1 1] loading axis to be $2.59 \times 10^{14}\ m^{-2}$ by making the necessary geometrical adjustments (see Appendix A). While this method is an approximation rather than a precise DD calculation, it would be reasonable for the dislocation density to increase by a factor no greater than ~3 because the increase in dislocation density is mainly caused by piling up the limited number of mobile dislocations against the pillar–coating interface.

We first calculated the effects of dislocation multiplication numerically, with the total number of samples greater than 1000. For the initial dislocation density of $10^{14}\ m^{-2}$, the SAS strength, σ_{SAS} in Eq. (1), was calculated to be 491 MPa. This value can be regarded as the yield strength without any coating effects ($\sigma_{SAS,uncoated}$). With coating, we know from DD simulations that the dislocation density increases up to $2.59 \times 10^{14}\ m^{-2}$, leading to a SAS strength of 552 MPa. This strength represents purely the effect of dislocation density increase ($\sigma_{SAS,uncoated}$). Therefore, the additional strengthening due to dislocation multiplication, $\Delta\sigma_{multiplication}$, was:

$$\Delta\sigma_{multiplication} = \sigma_{SAS,coated} - \sigma_{SAS,uncoated} = 61\ \text{MPa}.$$

$\Delta\sigma_{coating}$ was then determined by subtracting σ_{SAS} at the higher dislocation density from the maximum experimentally determined strength of $\sigma_{max,exp} = 1129$ MPa:

$$\Delta\sigma_{coating} = \sigma_{max,exp} - \sigma_{SAS}(\rho_{tot} = 2.59 \times 10^{14}\ m^{-2}) = 577\ \text{MPa}.$$

We found $\Delta\sigma_{multiplication}$ to represent ~5.4% of the overall strength and $\Delta\sigma_{coating}$ ~51% of the overall strength at the maximum strength level, 1129 MPa, which implies that the enhanced maximum strength of the coated nanopillars was caused mainly by dislocation pinning and pile-up at the hard coating rather than by dislocation multiplication. This significant strengthening by coating also agrees with the results captured by simple DD simulations shown in Section 4.1.1. Therefore, dislocation pinning and pile-up enhances the strength of nanopillars significantly.

4.2. The increase in dislocation density in D ~ 200 nm coated nanopillars

The bright-field TEM image of a deformed coated nanopillar 200 nm in diameter, shown in Fig. 6b, as well as the streaky diffraction pattern, shown in the inset, reveal a dislocation cell structure, accompanied by a significant increase in dislocation density as compared with the as-fabricated samples in Fig. 6a. Estimating the dislocation density based on these TEM images is challenging because of the highly interwoven dislocation segments within the cell walls. It is reasonable to assume that the dislocation density in the deformed coated pillars is similar to that of

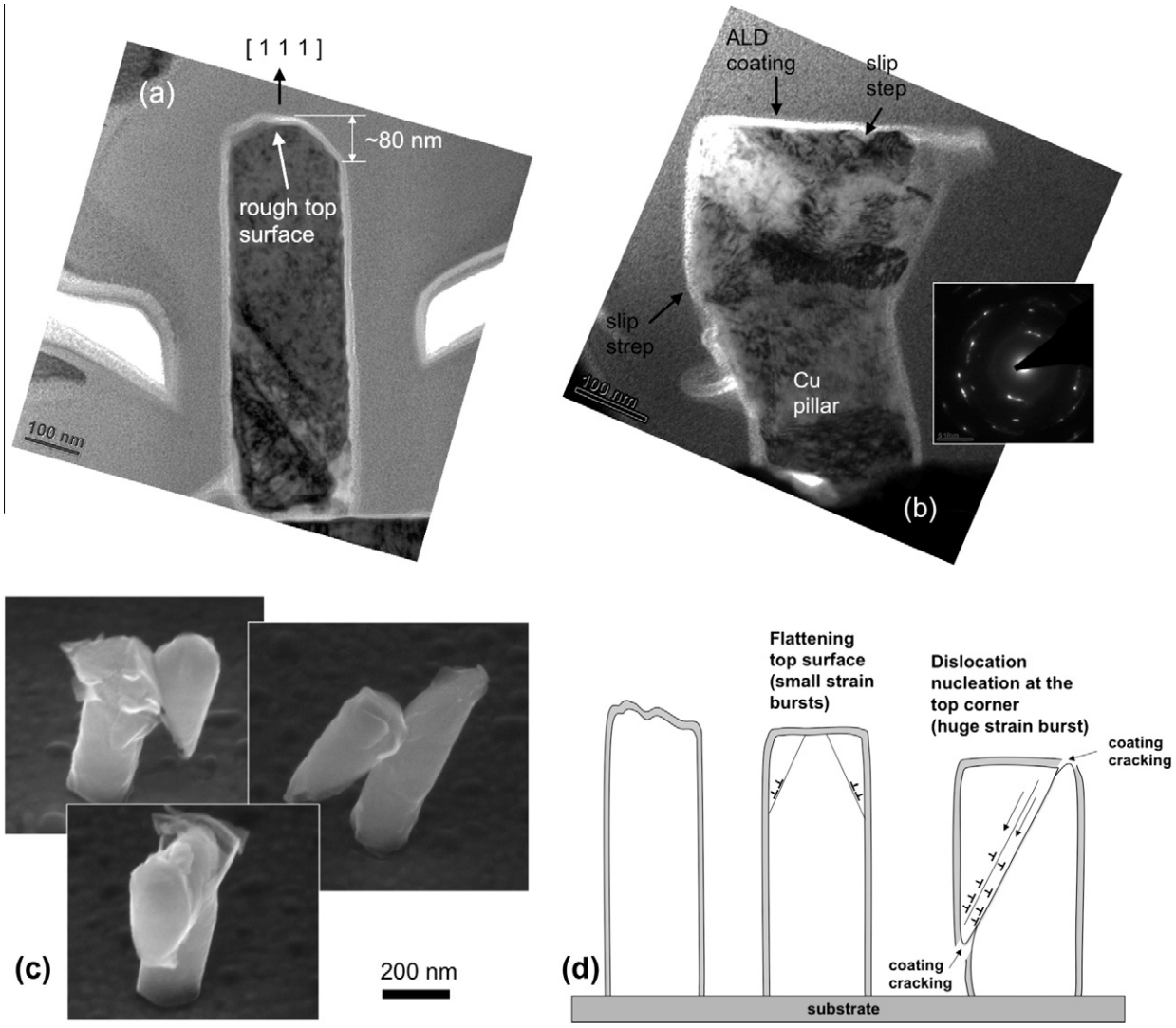

Fig. 6. Bright-field TEM image of coated Cu nanopillar (a) before and (b) after compression (Reprinted with the permission of Jennings et al. [27], copyright 2012, Acta materialia). (c) SEM images of coated Cu nanopillars after compression. All these samples are severely dislocated from the top corner. The flattening on the top part of the left image might occur right after dislocation nucleation at the top corner. (d) Schematic diagram of deformation mechanisms of coated Cu nanopillars.

a typical cell boundary, $\sim 10^{15}$–$10^{16}\,m^{-2}$, a value one or two orders of magnitude higher than that in the undeformed pillars. Our simulations showed that the presence of a hard coating caused only a factor of ~3–4 increase in the dislocation density even at the maximum compressive flow stress of 1.2 GPa and with the over-multiplication condition by cross-slip as described in Section 2.3. The injection of a large number of dislocations probably occurred during the substantial strain burst at the maximum flow stress in the experimental stress–strain data. Fig. 4c shows such a representative strain burst of ~30% strain.

Conventional breeding mechanisms may not be able to explain how such a large density of dislocations was produced in the small nanopillar volumes, in contrast to the report by Ng and Ngan, who demonstrated the increased dislocation densities and cell formation in compressed 6 μm diameter W-coated Al cylinders. In their samples, the multiplication probably occurred via the classical breeding mechanism, whereby cross-slipped dislocations, ubiquitously positioned throughout the sample, frequently interacted with mobile dislocations. This scenario is unlikely to have occurred in the nanopillars studied here. For a given initial dislocation density of $10^{14}\,m^{-2}$, the mean spacing of dislocations in the nanopillars is of the order of 100 nm, which represents half of the pillar diameter. Such a substantial interdislocation spacing would result in a higher probability of the mobile dislocations being piled-up at the pillar surface–coating interface than of interacting with one another. The simulations shown in Fig. 4b demonstrate that most of the cross-slipped dislocations were piled-up at the interface immediately after a single cross-slip event, with no further interactions with other dislocations. Even with the relatively low threshold for

cross-slip, which facilitated frequent attempts to cross-slip, the dislocation density in the simulations remained an order of magnitude lower than that in the experiments. This suggests that, unlike in the micron-sized pillars, cross-slip followed by dislocation interactions does not represent a viable mechanism for the extensive dislocation network formation in the 200 nm diameter nanopillars.

The DD simulation revealed that the motion of the pre-existing dislocations produced non-extensive strain bursts. In experiments, larger strain bursts could be observed if the coating contained localized micro- and nanocracks, which would unocclude a portion of the original free surface and enable dislocations to annihilate in that region. It is unlikely, therefore, that the operation of the pre-existing SASs caused the observed increase in dislocation density. To obtain both the significant increase in dislocation density and large strain bursts, which are thought to represent the extent of dislocation avalanches, additional sources of dislocations must operate. Jennings et al. previously demonstrated that the activation volumes of $1b^3$–$10b^3$ calculated from the constant strain-rate experiments on 75 and 125 nm diameter Cu nanopillars with the same loading orientation were consistent with surface dislocation nucleation [41]. These samples deformed at high compressive stresses, in excess of ~1 GPa, which are comparable to the maximum strengths of 1129 ± 201 MPa attained by the coated $D \sim 200$ nm Cu nanopillars studied here. Therefore, the stresses within the coated pillars are sufficiently high to nucleate dislocations at the interface. The maximum stress in the coated nanopillars is slightly higher than that for the reported surface nucleation stress in the uncoated nanopillars. This may be explained by the difficulty of dislocation nucleation at the metal–coating interface because the hard ALD Al_2O_3/TiO_2 inhibits local crystallographic slip at the interface due to the compatibility with the hard ceramic coating.

The TEM image in Fig. 6b shows pronounced slip traces, which emanated from the top cylinder rims, the locations of high stress concentrations. These stress concentrators might have facilitated heterogeneous nucleation of numerous dislocations that carried this deformation. SEM images of typical post-deformation pillar morphology, shown in Fig. 6c, demonstrate that the top corner-initiated slip is a common phenomenon in these samples. Dislocation nucleation at the metal–coating interface was probably facilitated by the substantial pile-ups of mobile dislocations followed by the dislocation source shut-down in the $D \sim 200$ nm-coated pillars. This is in contrast to the physics of dislocation nucleation at the free surfaces, i.e. in the pillars with no passivation, which was reported to occur in similar-diameter uncoated samples [41]. Thus, heterogeneous nucleation could occur in spite of the completely different boundary conditions. In the presence of hard coating, both the mobile dislocation pile-ups and pinning at the interface eventually drive the samples to contain insufficient numbers of mobile dislocations, which leads to heterogeneous dislocation nucleation. In contrast, without a hard coating, dislocation annihilation at the free surface leads to insufficient numbers of mobile dislocations, leading to dislocation nucleation at the free surface.

Fig. 6d describes the possible phenomenological sequence of events during the deformation of coated nanopillars with some roughness on the top. As described in Fig. 6d, some dislocations would be also introduced at the initial stage of loading before the stress reaches the maximum level. The flattened rough top surface could cause dislocation nucleation even at the lower applied stress. This argument is consistent with the sufficient plastic deformation at the low stress level as seen in Fig. 4c. Note that these initially introduced dislocations could play an important role in Bauschinger effects in the first unloading–loading cycle. A detailed analysis is given in the next section.

4.3. Bauschinger effects in $D \sim 200$ nm coated nanopillars

To compare the Bauschinger effect between simulations and experiments, the loop width was measured at the stress defined by $(\sigma_{unload} + \sigma_{reload})/2$, where σ_{unload} is the stress at the beginning of the unloading segment and σ_{reload} is the stress at the beginning of reloading for a given cycle, as schematically shown in Fig. 4c for the second cycle. The unloading–reloading axis in the simulations ([0 0 1]) is different from that in the experiments ([1 1 1]). Fig. 7a shows that a shear displacement of one Burgers vector (b) produces a single axial displacement, $b\cos(45°)$ for [0 0 1] axis and $b\cos(35°)$ for [1 1 1] axis, which means that the axial displacement of a [1 1 1]-oriented sample is 1.16 times larger than that of the [0 0 1] oriented ones. No other axial displacements exist due to crystallographic restrictions. Both the experimentally measured loop widths divided by 1.16 and the simulated loop widths of the first and second cycles are shown in Fig. 7b. Note that the effect of critical resolved shear stress (σ_{CRSS}) has not yet been considered.

For the first cycle, the peak stress of experiment is ~350 MPa [27], which corresponds to $\sigma_{CRSS} = 95.2$ MPa, and that of simulation is ~500 MPa, which corresponds to $\sigma_{CRSS} = 204$ MPa. Thus, σ_{CRSS} obtained from experiment is much lower than the simulated value. In other words, the applied stress in experiments is not high enough to cause sufficient amount of dislocation pile-ups, which eventually leads to the Bauschinger effect. However, Fig. 7b underlines that the experiments show a much more pronounced Bauschinger effect as compared with the simulations in the first cycle. As discussed at the end of the previous section, this is probably a result of the additional dislocation pile-ups formed during the compression of the non-flat pillar tops, illustrated in Fig. 6a and d, which shows that the top surface was not flat within ~80 nm range from the top apex of the sample. Thus, stress concentration at the irregular top surface would produce dislocations even at low applied stress. The stress–strain data in Fig. 4c shows that yielding and some plasticity occurred even before the first loading–reloading cycle, whereas the

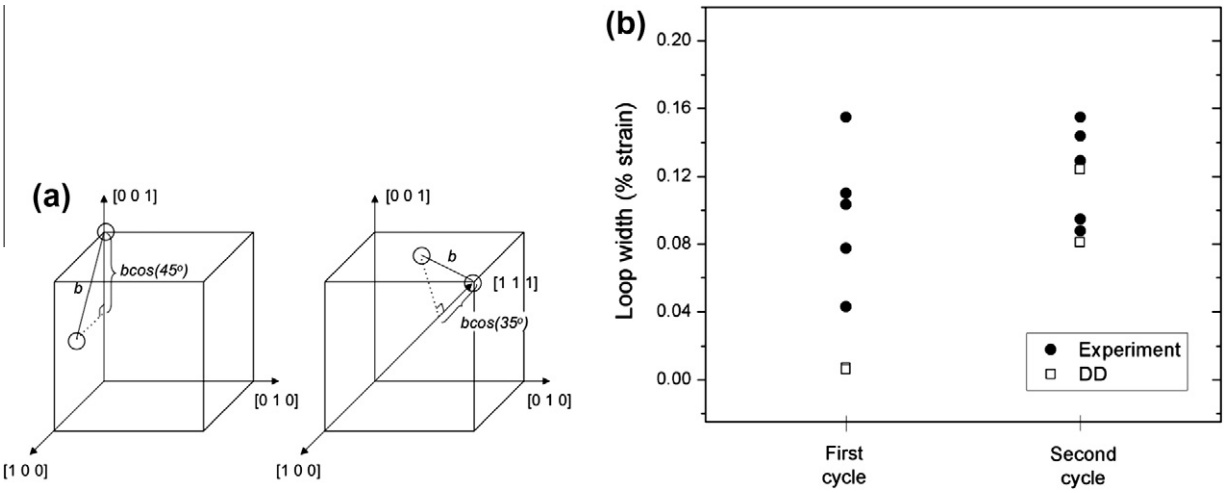

Fig. 7. (a) Schematic diagram of axial displacement for one Burgers vector displacement. (b) Loop widths of the first and second cycles in simulations and experiments.

simulated stress–strain curves were virtually fully elastic prior to the first such cycle. The back-stresses generated by the piled-up dislocations, which were formed during the flattening of the pillar tops, probably drove the Bauschinger effect in the first unloading–reloading cycle in the experiments. The substantial data scatter in the first cycle is consistent with this explanation because it arises from the differences in the top surface roughness among the samples. Additional dislocation pile-ups are also expected to occur in the vicinity of the top and bottom surfaces due to platen constraints. In contrast, the simulations were performed on idealized pillar geometries and did not suffer from similar boundary conditions, which is consistent with the first cycle showing a negligible loop width in Fig. 7b. Both simulations and experiments exhibited a noticeable Bauschinger effect in the second cycle. The applied stress of approximately 800 MPa during the second cycle in the simulations is sufficiently high for the dislocations to pile-up against the interface. The Bauschinger effect has been reported to be a function of pre-strain, with higher hysteresis widths occurring at larger strains [26,41]. Fig. 7b shows that the simulated Bauschinger effect, i.e. the loop width, in the second cycle is eight times greater than that in the first cycle, but shows that the experimental loop width is relatively similar between the first and second cycles. This marginal discrepancy was probably caused by geometrical imperfections in the samples.

5. Concluding remarks

We performed 3-D discrete DD simulations (ParaDiS) of uniaxial compressed Cu cylinders, which were conformally coated with a hard passivation layer. The results of these simulations were directly compared with the previously reported experimental findings on a nominally identical material system. In the experiments, 200 nm diameter single-crystalline Cu nanopillars, fabricated by templated electroplating, were passivated with ~10 nm of Al_2O_3 by ALD and quasi-statically compressed with several unloading–reloading cycles in the course of deformation. In the simulations, the impenetrable boundary condition was applied to mimic the hard ceramic coating layer such that the outward radial mobility of dislocations vanished within 5*b* from the free surface. DD simulations demonstrated that the dislocation density increased from 10^{14} to 3–4 $\times$ 10^{14} m^{-2} as the applied stress increased to its maximum value of 1.2 GPa at a strain of 1.2%. The originally proposed SAS model was modified to take into account the effects of dislocation pinning and pile-up at the interface. The modified model predicted the strengthening due to dislocation multiplication, $\Delta\sigma_{multiplication}$, to be 61 MPa, and the strengthening due to the presence of the coating, $\Delta\sigma_{coating}$, to be 577 MPa for the [1 1 1] loading axis. DD simulations revealed that the dislocation sources were pinned at the interface, which led to a higher line tension being required to operate the sources. The piled-up dislocations generated significant back-stresses, which prevented subsequent operation of the single-arm dislocation sources. These results suggest that the enhanced maximum strength of the coated nanopillars was a result of the dislocation pinning and pile-up processes due to the presence of an interface between the metal surface and the hard coating. This mechanism is distinct from the dislocation multiplication-driven strengthening that was observed in large micropillars [29].

TEM images of deformed coated nanopillars revealed a significant increase in the dislocation density and the formation of dislocation cell wall structures. The DD simulations demonstrated that the pre-existing dislocation sources were not capable of producing such a high dislocation density because the back-stress induced by the piled-up dislocations shut down the operation of dislocation sources. The operation of additional dislocation sources was necessary to increase the dislocation density. TEM and SEM images confirmed that the extensive slip events were initiated at the top corner of the sample where the stress was

highly concentrated. The experimentally measured maximum strength was comparable with the stresses required for the surface nucleation of dislocations in the uncoated Cu nanopillars, as reported in Ref. [27]. We postulate that the substantial strain bursts, which occurred at the highest applied stress, were likely caused by the spontaneous heterogeneous nucleation and propagation of dislocations in an avalanche fashion.

The effects of unloading–reloading hysteresis, i.e. the Bauschinger effect, were also analyzed and compared with experiments in detail. Experimental stress–strain data contained a noticeable Bauschinger effect in the first cycle, performed at ~400 MPa, whereas the loop width at the same stress in the simulations was negligible. We attributed this discrepancy to the formation of multiple dislocation pile-up arrays in the experiments prior to the first unloading–reloading cycle due to the non-ideal sample geometry. Both experiments and simulations displayed similar loop widths of ~0.12 strain for the second cycle, which was performed at a stress of ~800 MPa. The Bauschinger effect was more pronounced at higher strains, probably because of the greater number of piled-up dislocations at higher applied stresses at those strains.

Acknowledgements

The authors gratefully acknowledge the financial support of the Kavli Nanoscience Institute (KNI) fellowship and of the W.M. Keck Institute for Space Studies at Caltech. S.W.L. acknowledges the infrastructure and support of the KNI for carrying out the experiments.

Appendix A. Estimation of dislocation density for the [1 1 1] loading axis

In coated nanopillars, the dislocation density increases mostly by dislocation pile-up near the elliptical perimeter of slip plane as seen in Fig. 4b. Thus, the increase in dislocation density would be proportional to the circumference of elliptical slip plane. Furthermore, the increase in dislocation density is proportional to the number of active slip planes since mobile dislocations on active slip planes can be piled-up. Also, for a similar axial strength (simulation 1.2 GPa; experiment 1.129 GPa), the ratio of Schmid factors would be a proportional factor. The length of piled-up dislocations increases as the critical resolved shear stress increases since the higher stress drives dislocation sources to deposit more dislocations near the interface. Thus, the ratio of Schmid factor must be taken into account. Now, the increase in dislocation density for the [1 1 1] loading axis can be roughly estimated as:

$$\Delta\rho_{[111]} \approx \Delta\rho_{[001]} \times \frac{C_{[111]}}{C_{[001]}} \times \frac{P_{[111]}}{P_{[001]}} \times \frac{M_{[111]}}{M_{[001]}} \quad (2)$$

where $\Delta\rho_{[111]}$ is the estimated increase in dislocation density for the [1 1 1] loading axis, $\Delta\rho_{[001]}$ the increase in dislocation density for the [0 0 1] loading axis, C is the circumference of the elliptical slip plane, M is the Schmid factor, and P is the number of active slip plane. The subscripts of C and P indicate the direction of loading axis. C is defined approximately as $2\pi\sqrt{\frac{D_{major}^2+D_{minor}^2}{2}}$, where D is the length of the axis of the ellipse. For pillar geometry, D_{minor} is same with the pillar diameter, D, and $D_{major} = D\cos\theta$, where θ is the angle between the loading axis and the major axis of elliptical slip plane. Thus, $\theta_{[111]} = 19.5°$ and $\theta_{[001]} = 35.3°$, where the subscript represents the direction of the loading axis. Then, Eq. (2) becomes:

$$\begin{aligned}\Delta\rho_{[111]} &\approx \Delta\rho_{[001]} \times \sqrt{\frac{\cos^2(19.3)+1}{\cos^2(35.3)+1}} \times \frac{3}{4} \times \frac{0.272}{0.408} \\ &\approx \Delta\rho_{[001]} \times 0.53.\end{aligned}$$

The increase in dislocation density for [0 0 1] loading axis is:

$$\begin{aligned}\Delta\rho_{[001]} &= \Delta\rho_{[001],final} - \Delta\rho_{[001],initial} = (4-1)\times 10^{14} \\ &= 3\times 10^{14}\ \mathrm{m}^{-2}.\end{aligned}$$

Then, the estimated total dislocation density for the [1 1 1] loading axis at the maximum stress state would be:

$$\begin{aligned}\rho_{[111]} &= \rho_{[111],initial} + \Delta\rho_{[111]} = 10^{14} + (3\times 10^{14} m^{-2}) \times 0.53 \\ &= 2.59\times 10^{14}\ \mathrm{m}^{-2}.\end{aligned}$$

Appendix B. Supplementary material

Supplementary data associated with this article can be found, in the online version, at http://dx.doi.org/10.1016/j.actamat.2012.12.008.

References

[1] Nix WD, Greer JR, Feng G, Lilleodden ET. Thin Solid Films 2007;515:3152.
[2] Gil Sevillano J, Ocaña Arizcorreta I, Kubin LP. Mater Sci Eng A 2001;309-310:393.
[3] Uchic MD, Dimiduk DM, Florando JN, Nix WD. Science 2004;305:986.
[4] Greer JR, Oliver WC, Nix WD. Acta Mater 2005;53:1821.
[5] Volkert CA, Lilleodden ET. Philos Mag 2006;86:5567.
[6] Kiener D, Grosinger W, Dehm G, Pippan R. Acta Mater 2008;56:580.
[7] Kim J-Y, Greer JR. Acta Mater 2009;57:5245.
[8] Uchic MD, Shade PA, Dimiduk DM. Ann Rev Mater Res 2009;39:361.
[9] Kraft O, Gruber PA, Mönig R, Weygand D. Ann Rev Mater Res 2010;40:293.
[10] Greer JR, De Hosson JTM. Prog Mater Sci 2011;56:654.
[11] Dimiduk DM, Woodward C, LeSar R, Uchic MD. Science 2006;312:1188.
[12] Csikor FF, Motz C, Weygand D, Zaiser M, Zapperi S. Science 2007;318:251.
[13] Brinckmann S, Kim J-Y, Greer JR. Phys Rev Lett 2008:100.
[14] Ng KS, Ngan AHW. Acta Mater 2008;56:1712.
[15] Zaiser M, Schwerdtfeger J, Schneider AS, Frick CP, Clark BG, Gruber PA, et al. Philos Mag 2008;88:3861.
[16] Friedman N, Jennings AT, Tsekenis G, Kim J-Y, Tao M, Uhl JT, et al. Phys Rev Lett 2012;109:095507.

[17] Rao SI, Dimiduk DM, Tang M, Parthasarathy TA, Uchic MD, Woodward C. Philos Mag 2007;87:4777.
[18] Ng KS, Ngan AHW. Scripta Mater 2008;59:796.
[19] Rao SI, Dimiduk DM, Parthasarathy TA, Uchic MD, Tang M, Woodward C. Acta Mater 2008;56:3245.
[20] Lee S-W, Nix WD. Mater Sci Eng A 2010;527:1903.
[21] Lee S-W, Nix WD. Philos Mag 2012;92:1238.
[22] Mompiou F, Legros M, Sedlmayr A, Gianola DS, Caillard D, Kraft O. Acta Mater 2012;60:977.
[23] Greer JR, Nix WD. Phys Rev B 2006:73.
[24] Lee S-W, Han SM, Nix WD. Acta Mater 2009;57:4404.
[25] Zheng H, Cao A, Weinberger CR, Huang JY, Du K, Wang J, et al. Nat Commun 2010:1.
[26] Nicola L, Xiang Y, Vlassak JJ, Van der Giessen E, Needleman A. J Mech Phys Solids 2006;54:2089.
[27] Jennings AT, Gross C, Greer F, Aitken ZH, Lee SW, Weinberger CR, et al. Acta Mater 2012;60:3444.
[28] Greer JR. Mater Res Soc Symp 2007. 0983-LL08-03.
[29] Ng KS, Ngan AHW. Acta Mater 2009;57:4902.
[30] Zhou C, Biner S, LeSar R. Scripta Mater 2010;63:1096.
[31] El-Awady JA, Rao SI, Woodward C, Dimiduk DM, Uchic MD. Int J Plast 2011;27:372.
[32] Arsenlis A, Cai W, Tang M, Rhee M, Oppelstrup T, Hommes G, et al. Model Simul Mater Sci Eng 2007;15:553.
[33] Weinberger CR, Cai W. J Mech Phys Solids 2007;55:2027.
[34] Yoffe EH. Philos Mag 1961;6:1147.
[35] Weinberger CR, Aubry S, Lee S-W, Nix WD, Cai W. Model Simul Mater Sci Eng 2009:17.
[36] Tang M, Cai W, Xu G, Bulatov VV. Model Simul Mater Sci Eng 2006;14:1139.
[37] Tang H, Schwarz KW, Espinosa HD. Phys Rev Lett 2008:100.
[38] Verdier M, Fivel M, Groma I. Model Simul Mater Sci Eng 1998;6:755.
[39] Espinosa HD, Panico M, Berbenni S, Schwarz KW. Int J Plast 2006;22:2091.
[40] Zhou C, Biner SB, LeSar R. Acta Mater 2010;58:1565.
[41] Jennings AT, Li J, Greer JR. Acta Mater 2011;59:5627.
[42] Lee SW, Aubry S, Nix WD, Cai W. Model Simul Mater Sci Eng 2011;19:025002.
[43] Motz C, Weygand D, Senger J, Gumbsch P. Acta Mater 2009;57:1744.
[44] Zhu T, Li J, Samanta A, Leach A, Gall K. Phys Rev Lett 2008:100.
[45] Gu R, Ngan AHW. Acta Mater 2012;60:6102.